

# Surface currents and significant wave height variability: a numerical investigation of the Agulhas current region

Gwendal Marechal<sup>1</sup> and Fabrice Ardhuin<sup>2</sup>

<sup>1</sup>Univ. Brest, CNRS, Ifremer, IRD, Laboratoire d’Océanographie Physique et Spatiale, Brest, France

<sup>2</sup>Univ. Brest

November 26, 2022

## Abstract

Advances in the understanding and modelling of surface currents have revealed the importance of internal waves, mesoscale and submesoscale turbulence. Indeed all these features should have a large influence on wind waves, and in particular wave heights are expected to be modified by refraction. Still, the quantitative impact of currents on waves is not well known due to the complexity of the random wave fields and currents that are found in the ocean, and the lack of observations of both currents and waves at scales shorter than 150 km. Here we use novel satellite altimetry data and state of the art phase-averaged numerical wave models forced by currents at different resolutions in the Agulhas region. We find that a numerical wave model that uses surface currents with resolutions of 30 km or less and a directional resolution of 7.5 ° or less, can provide accurate representations of the significant wave height gradients found in the Agulhas current. Using smoother current fields, such as derived from satellite altimetry alone, generally underestimates gradients and extreme wave heights. This work suggests that high resolution satellite altimetry data can be combined with numerical wave models to provide a statistical validation of surface current gradients.

# Surface currents and significant wave height variability: a numerical investigation of the Agulhas current region

Gwendal Marechal<sup>1</sup>, Fabrice Ardhuin<sup>1,2</sup>

<sup>1</sup>Univ. Brest, CNRS, Ifremer, IRD, Laboratoire d'Océanographie Physique et Spatiale, Brest, France

<sup>2</sup>Scripps Institution of Oceanography, University of California, La Jolla, CA, USA

## Key Points:

- Spatial resolution of currents is key for reproducing wave height gradients
- 30 km resolution over the Agulhas current is necessary to retrieve most of the observed gradients
- Incident waves with a narrow directional spreading induce larger wave height gradients

---

Corresponding author: Gwendal Marechal, [gwendal.marechal@ifremer.fr](mailto:gwendal.marechal@ifremer.fr)

## Abstract

Advances in the understanding and modelling of surface currents have revealed the importance of internal waves, mesoscale and submesoscale turbulence. Indeed all these features should have a large influence on wind waves, and in particular wave heights are expected to be modified by refraction. Still, the quantitative impact of currents on waves is not well known due to the complexity of the random wave fields and currents that are found in the ocean, and the lack of observations of both currents and waves at scales shorter than 150 km. Here we use novel satellite altimetry data and state of the art phase-averaged numerical wave models forced by currents at different resolutions in the Agulhas region. We find that a numerical wave model that uses surface currents with resolutions of 30 km or less and a directional resolution of  $7.5^\circ$  or less, can provide accurate representations of the significant wave height gradients found in the Agulhas current. Using smoother current fields, such as derived from satellite altimetry alone, generally underestimates gradients and extreme wave heights. This work suggests that high resolution satellite altimetry data can be combined with numerical wave models to provide a statistical validation of surface current gradients.

## 1 Introduction

Surface gravity waves generated by wind (hereinafter waves) interact with surface currents at all scales due to a wide range of processes (Phillips, 1977). In the ocean, it appears that refraction, which focuses wave energy in current jets that flow in the wave direction, is probably the dominant source of variations of wave heights at scales 50 to 200 km (Ardhuin et al., 2017). For currents speeds much weaker than the waves phase speed it is the rotational part of the current that is expected to explain the variations in wave directions (Landau & Lifshitz, 1960; Villas Bôas & Young, 2020). This refraction can lead to extreme wave heights over large mesoscale currents, such as the Agulhas current, that are dangerous for ships and off-shore structures (Gutshabash & Lavrenov, 1986). Other impacts of waves on air-sea fluxes, upper ocean mixing or remote sensing also require better knowledge on wave-current interactions (e.g. D’Asaro, 2014; Sandwell et al., 2014; Villas Bôas et al., 2019).

Recent advances in understandings and in ocean modeling of surface ocean dynamic show that the upper ocean is highly energetic at the mesoscale, for which the flow is in quasi-geostrophic balance, but also at smaller scales (submesoscales) (McWilliams, 2016). Further, strong ocean currents are associated with sharp and asymmetric velocity fronts, with larger positive vorticity maxima in the Northern hemisphere (e.g. Gula et al., 2015). Also, the generation of large surface waves has been shown to occur in the presence of strong internal waves (Osborne & Burch, 1980). All these small scale current features may contain as much surface kinetic energy (KE) as the mesoscales but it is not clear how much they influence the waves. Refraction theory tells us that changes in wave direction for a given wave frequency are the product of the current vorticity magnitude and the scale of the current feature, so that a localized high vorticity may have the same effect as a distributed but lower vorticity. But in practice, ocean waves are random and the different components of their relatively broad spectrum are affected in different ways by the surface vorticity.

The evolution of the wave field, represented by the wave action spectral densities  $N(\sigma, \theta)$ , with  $\sigma$  the wave frequency in the frame of reference moving with the local current and  $\theta$  the wave propagation direction generally follows the wave action equation (Komen et al., 1994; Tolman & Booij, 1998),

$$\partial_t N + \partial_\lambda(\dot{\lambda}N) + \partial_\phi(\dot{\phi}N) + \partial_\sigma(\dot{\sigma}N) + \partial_\theta(\dot{\theta}N) = \frac{S}{\sigma} \quad (1)$$

The contributions of surface currents in equation (1) come into the advection speeds in longitude  $\dot{\lambda}$  and latitude  $\dot{\phi}$ , which is the sum of the intrinsic group speed and the sur-

face current, the refraction velocity  $\dot{\theta}$ , the change of frequency velocity  $\dot{\sigma}$ , and in the right-hand-side source term  $S$  because the effective wind velocity that generates waves is the vector difference of wind and surface current velocities (e.g., Ardhuin et al., 2017).

Because the effect of refraction  $\dot{\theta}$  at position  $(\lambda, \phi)$  combines with the advection in a new direction  $\theta$  to produce a change in wave action  $N$  at another location  $(\lambda', \phi')$ , there is no simple relationship between the current field and wave field, in other words, surface currents have a non local effect on the distribution of the wave action in the current field.

White and Fornberg (1998) have shown theoretically that the spatial distribution of refraction-induced focusing can be predicted for monochromatic waves over a random current with a narrow band spectrum. Still, that does not say much about the spatial distribution of wave heights in this case. The problem is more complex for broad band current spectrum and random waves, for which the wave height combines all the spectral components,

$$H_s = 4 \sqrt{\int_0^\infty \int_0^{2\pi} \sigma N(\sigma, \theta) d\theta d\sigma}. \quad (2)$$

Guided by these theoretical insights and the solid foundation of the Wave Action Equation (e.g. White, 1999), our understanding of the effects of surface currents on wave height in the real ocean has relied on numerical simulations using eq. (1). These simulations are fairly successful for well-known tidal currents (e.g. Ardhuin et al., 2012), but there are very little data to validate modeled currents and waves in other regions. For example, wave simulations in the Gulf Stream and Drake Passage suggest that the patterns of  $H_s$  field induced by surface currents is dominated by the refraction (Ardhuin et al., 2017), with a significant impact of small scale currents. These modelling results could not be validated using standard satellite altimeter data that is dominated by noise for along-track wavelengths shorter than 100 km (Dibarboure et al., 2014). The development of new de-noising techniques has revealed a systematic relation between wave height gradients and current vorticity (Quilfen et al., 2018; Quilfen & Chapron, 2019). These filtered data have been compared to preliminary simulations in the Agulhas current using eq. (1) solved by either finite difference techniques or ray tracing. These comparisons have highlighted the importance of the directional width of the wave spectrum, with stronger  $H_s$  gradients obtained for narrower incident wave spectra even when only large scale currents, as derived from gridded altimetry data were used (Quilfen et al., 2018).

These two previous studies by Ardhuin et al. (2017) and Quilfen et al. (2018) have suggested two possible reasons for sharp  $H_s$  gradient: namely the presence of sharp current gradients, or the strong local focalisation of waves on a smooth current field. Figure 1 illustrates the first possibility over the Agulhas current, using either large-scale currents of gridded altimetry or a high resolution modeled current, both described in detail in section 2.

The present work aims at consolidating these previous analyses and contribute to answering the questions: What are the parameters controlling the spatial variability of wave heights in a realistic current field? How can these be best reproduced by numerical models? In particular, we focus on the effect of the spatial resolution of the current field, and angular discretization of the wave model in relation with the directional spread of wave spectra. Here we focus on the Agulhas current because of the strong  $H_s$  signature that is easily captured by satellite altimeters. Further work will be needed for other wave and current regimes.

The numerical model set up and data are presented in section 2. Results follow in section 3, with a discussion of the influence of the surface currents resolution in section 4. Finally we will conclude this wave-current interactions study in section 5.

## 2 Satellite and modelling data for waves in the Agulhas current

The Agulhas current system is one of the most intense western boundary currents, with velocities exceeding  $2.5 \text{ m s}^{-1}$  along the East coast of South Africa, before retroflecting back into the Indian Ocean with large ring eddies shed in the south Atlantic ocean (Beal et al., 2011; Tedesco et al., 2019). The Agulhas current system is also exposed to very large waves from the southern ocean (Young, 1999).

### 2.1 High-resolution altimetry $H_s$ data

Satellite altimeters have been measuring  $H_s$  continuously for 27 years, providing measurements along sparsely spaced tracks, typically every 10 to 30 days (Ardhuin et al., 2019). In many regions of the ocean these are the only available measurement of wave heights. This is particularly the case in strong current regions where moored buoys are more difficult to install. Further,  $H_s$  measurements along the satellite ground track provide a unique view of the spatial variations of  $H_s$ , although along one dimension only. Until recently, the analysis of  $H_s$  variations was limited to wavelengths larger than 100 km, due to the noise associated to the tracking methods used to interpret altimeter waveforms (Sandwell et al., 2014; Ardhuin et al., 2017). The successful application of Empirical Mode Decomposition (Huang et al., 1998) to the denoising of  $H_s$  along-track series now makes it possible to investigate much smaller scales, possibly down to 15 km wavelength or less (Quilfen & Chapron, 2019). Here we use denoised wave heights from the European Space Agency (ESA) Sea State Climate Change Initiative (SeaState-CCI) database, that uses this denoising technique applied to calibrated Geophysical Data Records from CNES and ESA for the Jason-2, Cryosat-2 and SARAL/AltiKa missions. The analysis of three years from 2014 to 2016 in our region of interest gives a total of 4746 satellite tracks, with one example shown in Fig. 1.

### 2.2 Numerical wave model

Our numerical wave model is based on the WAVEWATCH III modelling framework (The WAVEWATCH III<sup>®</sup> Development Group, 2016) that integrates the action balance equation (1), discretized on a regular latitude-longitude grid with a resolution of  $1/30^\circ$ . Our baseline configuration uses a spectral discretization into 32 frequencies from 0.037 Hz to 0.7 Hz and 48 directions ( $\Delta\theta = 7.5^\circ$ ). This model is forced by surface currents, as detailed below, together with operational hourly wind forecasts from the European Centre for Medium-Range Weather Forecasts (ECMWF), at  $1/8^\circ$  resolution. The overall time step used to solve eq. (1) is 390 s, and the solution is obtained with a splitting technique (Tolman, 1992), with a spatial advection step of 130 s, a refraction step of 18 s, and an automatically adjusted source term integration step that can be as short as 10 s. We forced the boundaries three hourly by waves spectra from a global model configuration that uses the same wind fields but no current, a spatial resolution of  $0.5^\circ$  and the same spectral discretization as our Agulhas model. One example of modeled  $H_s$  field is shown in Fig. 1.

The signature of the Agulhas systems is clearly visible in the modeled  $H_s$  field with a band of larger wave heights. On the example in Fig. 1.a, one can observe the effect of the main Agulhas current along the coast, including a meander known as a "Natal pulse", located at  $29^\circ\text{E}$ , upstream of Port Elisabeth. Large current structures typically have multiple parallel branches caused by the straining of the large scale field and very sharp boundaries (Fig. 1.b). In contrast, the  $H_s$  field computed with the model using surface currents estimated from altimetry measurements (Globcurrent), has blurred patterns (Fig. 1.c), caused by surface currents with broader features and less intense maxima values (Fig. 1.d). Altimeter measurements show a narrow  $H_s$  maximum around  $37^\circ$  in the Agulhas current upstream of the retroflexion (Fig. 1.e). This narrow peak in  $H_s$  is closer

to the one obtained with the CROCO currents, while the Globcurrent current fields lead to a broad  $H_s$  maximum.

### 2.3 Currents fields used for forcing the wave model

Given the large influence of surface current details we have designed a series of simulations with currents at different resolutions. These current fields are based on surface current estimates from the Coastal and Regional Ocean COmmunity model (CROCO, Debreu et al., 2012) without data assimilation nor tidal forcing with a resolution of  $1/36^\circ$  both in latitude and longitude. This CROCO model configuration is expected to produce surface currents that are statistically consistent with the real ocean and has been used for several process studies (Tedesco et al., 2019). However, for any particular time and location, the variable current structure is not expected to reproduce the stochastic behaviour of the ocean as no data assimilation is used within the model domain. The CROCO model has been forced at the surface by the ERA-interim reanalysis and boundaries have been forced by a global reanalysis GLORYS. We have also used low-pass filtered CROCO currents as an input forcing for the wave model. These are obtained by applying an isotropic two-dimensional Gaussian filter defined by its standard deviation  $\sigma_c$  expressed in number of grid points.

The filtered current fields effective resolution is the result of the convolution of the Gaussian filter and the original current field. In particular the spectrum of the filtered current is the product of the original current spectrum and the spectrum of the Gaussian filter. The effective resolution is thus driven by the width of the Gaussian filter,  $\sigma_c$ . We performed a spectral analysis on all surface currents forcing fields (CROCO fully resolved and filtered). Rather than computed the fourier transform of the different current fields, we have done the spectral analysis on the laplacian applied both on the original surface currents and the gaussian filters. We computed the fourier transform along the zonal dimension and we folded the obtained spectra on themselves to removed the symmetric aspect. As previously stated for the filtered currents fields, we computed the product of the fourier transform of the fully resolved surface current and the different gaussian filters (according to the convolution theorem). Finally we took the averaged of all computed spectra. Hanning windows have been applied on all data-segments to avoid spectral leakage.

For filtered fields, scales smaller than where the KE laplacian PSD start to *bounce* (fig. 2) have been considered as removed by the gaussian filter. This scale-frequency cut-off defines the effective resolution of the filtered current field. The two different regimes (monotonic and non-monotonic) shown on spectra (fig. 2) are highly better noticeable when laplacian is applied both on the currents fields and the filters (spectra for the non-modified field, no laplacian applied, are not shown here.) Let's notice that the effective resolution found by the spectral analysis is (almost) equal to the width of the gaussian ( $2\sigma_c$ ) times the original surface current field pixel size ( $\Delta x = 2.5km$ ).

Seven surface currents fields have been created, with effective resolutions ranging from 10 to 100km. Figure 3 illustrates four patterns of currents with the vorticity  $\zeta = \partial V/\partial x - \partial U/\partial y$  and  $H_s$  corresponding to different current resolutions.

The filtering of the current field results in the removal of small scale structures, including small mesoscale eddies and filaments, as well as the smoothing of the large scale structures. Alternatively, we also used a surface current forcing taken from the Globcurrent product (Rio et al., 2014). This Globcurrent product has a spatial resolution of  $1/4^\circ$  both in latitude and longitude and is temporally resolved at 1 day. It provides the geostrophic component of the total surface currents estimated from the Sea Surface Height (SSH) measured by altimeters, and a mean dynamic topography that combines other data sources (Rio et al., 2014). A similar spectral analysis described above has been applied on Globcurrent product and revealed its effective resolution 150km. The 50 km resolution filtered

CROCO current has scales similar to those in the Globcurrent field, with a lower surface currents intensity for filtered surface current (due to filtering process). Let's notice that our filtered surface relative vorticity  $\zeta$  displayed in fig. 3 are similar to the ones presented in figure 17c of Chelton et al. (2019) in the Coastal California current for the similar resolution (few kilometers, 20km and 80km).

Snapshots of simulated  $H_s$  reveal patterns that follow the surface vorticity patterns as already shown in figure 13 of Quilfen et al. (2018). Figures (3 right) show a  $H_s$  maximum where the normalized vorticity is positive in the main stream of the Agulhas (south-westward) and also show that the  $H_s$  gradient are sharp for forcing using modeled (CROCO) currents and become blurred for poorly resolved surface current. We have run our wave model during 3 years, from 2014 to 2016, with the appropriate surface currents (fully resolved from CROCO model, filtered and estimated by altimetry), wind and boundary conditions forcings.

### 3 Results

#### 3.1 Spatial variability of $H_s$ in realistic surface currents field

Wave-current interactions have been simulated in the Agulhas current from 2014 to 2016. Filtered altimetry data have been studied for the same time frame and all model outputs have been interpolated in time and space on those altimeters tracks. One example of model-satellite comparison is displayed in figure (1e). Except for the topographically trapped flow patterns, the high resolution CROCO model is not expected to have current features in the same place as the real features, but it may still have realistic eddy sizes and meander shapes. We will thus compare the statistical properties of modeled and measured  $H_s$ .

In particular we consider the statistical properties of the along-track  $H_s$  gradient defined as

$$\nabla H_s = |\Delta H_s / dr|, \quad (3)$$

with  $dr$  the along-track distance between successive 1 Hz measurements ( $dr$  is typically 7 km), and  $\Delta H_s$  the difference between successive  $H_s$  measurements taken 1 s apart. Statistics of  $\nabla H_s$  have been interpolated on a regular grid with a resolution of  $1/8^\circ$  by  $1/8^\circ$  in longitude and latitude. The mean values are shown on figure 4, ranging from 0 to 3 cm per km.

Besides a few high values right at the coast (well visible for simulation without current) that can be explained by partial sheltering caused by headlands, all the large gradients appear in regions of strong current gradients, and specifically in the main Agulhas current, from  $29^\circ\text{E } 33^\circ\text{S}$  to  $17.5^\circ\text{E } 39^\circ\text{S}$ . The values of the mean  $\nabla H_s$  measured in the main Agulhas branch are in the range of 1.5 to 3 cm/km (Fig. 4.i.) which is remarkably high, and corresponds to the maximum values shown in Figure 1. These persistent maximum gradients are located exactly where the model has the strongest current, and where the largest  $H_s$  gradients are also predicted in figure 4.a. This is the well known region of strong focalization of waves caused by wave refraction over the current (Gutshabash & Lavrenov, 1986; Kudryavtsev et al., 2017; Quilfen & Chapron, 2019). Indeed when propagating against a current that is uniform in the flow direction, waves of a given period and direction can be trapped: when coming from the center of the current towards its edge they turn back towards the center at the location where the current reaches a certain value (Kenyon, 1971). The waves behaviour is similar to the propagation of light waves along an optical fiber where light waves are trapped and propagate within a range of specific refraction's index values that depends on their initial incidence angle. Quilfen and Chapron (2019) have demonstrated with ray tracing and assuming the wave action is conserved along the ray, that where waves are trapped, strong  $\nabla H_s$  are measured.



Figure 4 shows that the maximum  $\nabla H_s$  signal is upstream 26°E, where the main Agulhas current is known to be stable. Downstream of 26°E the current is bi-modal with occasional disturbances known as Natal pulses

Around 22°E the Agulhas current comes off the Agulhas Bank and the current direction veers to the south, which probably explains the lower values of  $\nabla H_s$  as the current direction is less favorable for trapping the dominant south-westerly waves, resulting in this lower gradient of wave heights. Beyond that point,  $\nabla H_s$  increases again but it is more spread out in the north-south direction.

Nowhere does the much coarser and weaker current in the Globcurrent product produces  $H_s$  gradients larger than 2 cm/km (Fig. 1.g). Yet, the Globcurrent product leads to modeled gradients in the retroflexion region, around 38° S, 25 °E, that are similar to those given by the CROCO model, both weaker than observed.  $\nabla H_s$  in the main Agulhas current are similar for CROCO filtered at 50km and Globcurrent, as shown in fig 3 through the  $H_s$  field. As the effective current resolution is degraded from 10 km to 50 km, the mean  $H_s$  gradient progressively vanishes with a particularly clear drop from 50 km (Fig. 1.e) to 70 km (Fig. 1.f).

### 3.2 Spectral analysis

In order to obtain a more quantitative analysis, we perform the same spectral analysis on the model and satellite data. We use overlapping windows following Welch (1967), with the Fourier transform computed after detrending and applying a Hanning window. Results are presented in Figure 5. In order to help with the interpretation, the surface current velocity ( $\sqrt{U^2 + V^2}$ ) was also analyzed along the same tracks. One spectrum is computed for each track. All spectra have been averaged to obtain one averaged spectrum for each numerical simulation for each surface currents forcing field. The  $H_s$  spectra (Fig. 5.a) show that between resolutions of 200 km and 30 km, and even down to the smaller resolved scale, the resolution of the surface currents drive the  $H_s$  variability. For wavelengths between 50 km and 100 km, simulations forced by the Globcurrent surface currents shows a  $H_s$  variability higher than simulations forced with surface currents filtered at 50km, 70km and 100km whereas surface currents from Globcurrent have an effective along-track resolution around 150km. This along-track resolution is consistent with the 150 to 250 km resolution of sea surface height gridded altimeter data in the Agulhas region (Ballarotta et al., 2019).

Using a wave model forced by different surface KE spectra (Fig. 5.b) reveal what we expected, i.e the lower the surface currents KE, the lower the  $H_s$  spectrum. Surface KE spectrum computed from surface current taken from Globcurrent fields show a level of variability for wavelengths in the range 50 to 200 km that is similar to the 40-km filtered current.

For all simulations, the shape of the  $H_s$  spectrum is very similar to the KE spectrum, and slightly steeper, around  $k^{-3.4}$  for  $H_s$  compared to  $k^{-3.0}$  for the KE spectrum. The same behavior was found for realistic simulation in Gulf-Stream and Drake Passage (Ardhuin et al., 2017). As the spectral level in the current forcing is reduced, the  $H_s$  spectrum is reduced in the same proportion until it reaches a background level. For a wavelength of 100 km, this background level is around 0.08 m<sup>2</sup>/cycle/km, which is very close to the variability associated to the wind field in the analysis by Ardhuin et al. (2017). This parallel behaviour of the  $H_s$  and KE spectra may be due to the dominant balance between propagation and refraction terms in the action balance equation (1).



## 4 Discussions and perspectives

### 4.1 Surface current resolution and gradients of $H_s$

In the ocean, surface currents are energetic at meso- and submesoscales, with features such as fronts, eddies and vorticity filaments. Waves interact with those features, and the refraction explains the spatial redistribution of the wave action density that results in a change of  $H_s$ . In the Agulhas system, waves simulations forced with highly resolved surface currents, rich in surface structures at meso- and submesoscale (left fig. 3 a,b) show that the small features matter to simulate realistic  $\nabla H_s$ , statistically consistent with filtered altimeter data (Fig 4). In the Agulhas, the long term study shows that the main part of the  $\nabla H_s$  is induced by intense surface structures smaller than 30km superimposed on the large scale Agulhas current system (Fig. 4). Recent idealised studies from (Villas Bôas & Young, 2020), reveal that for waves propagating much faster than currents, only the rotational component of the surface currents induces a scattering of wind wave. Filtering the surface currents results in a decrease of global surface vorticity due to the small and intense vorticity features removing and the decrease of the large scale mean vorticity (Fig. 3.c). Change the global vorticity impact the refraction intensity. Refraction seems to be the main process that drives the occurrence of  $\nabla H_s$  at meso- and submesoscale in strong mesoscale curr, already proved numerically in the Gulf-Stream and the Drake passage (Ardhuin et al., 2017). The choice of the surface currents forcing is also key to reproducing the strong realistic  $H_s$  variability. Quilfen et al. (2018) argued that numerical wave models that solve the action balance eq. (1) using finite differences, generally underestimate the  $\nabla H_s$ . Also, Quilfen et al. (2018) have shown marked differences between finite-differences and ray-tracing solutions. Here we find that it is the choice of a large scale current from Globcurrent that explains the relatively weak modeled  $H_s$  gradient.

### 4.2 Waves model directional resolution

In the limit of a large number of directions and a thin spatial resolution, the solution to the wave action equation obtained here with the 3rd order finite-difference refraction and advection schemes should be identical to the one obtained with backward ray tracing (Longuet-Higgins, 1957; O'Reilly & Guza, 1993; Booij et al., 1999; Ardhuin & Herbers, 2005). In practice, the number of discrete model directions is limited by the cost in memory storage and computation time, and most wave model implementations use 24 to 36 directions. Here, our wave model computes the wave spectrum  $E(f, \theta)$  in each grid-cell of the domain,  $E(f, \theta)$  decomposed in 32 wave frequencies and 48 directions.

Given the importance of refraction in the presence of current gradients (Holthuijsen & Tolman, 1991; Ardhuin et al., 2012) we examine here the importance of the directional resolution and how the numerical solution is smoothed by the use of a small number of directions. We have thus repeated our simulations (same forcing files and same boundary conditions) different directional resolutions ( $\Delta\theta$ ), using 24 ( $\Delta\theta = 15^\circ$ ), and 180 ( $\Delta\theta = 2^\circ$ ) directions instead of 48 ( $\Delta\theta = 7.5^\circ$ ). The refraction timestep  $\Delta t_r$  has been changed in proportion to keep a constant ratio  $\Delta t_r / \Delta\theta$ . We have further checked that reducing the other time steps had minimal effects on the solution. The spectral analysis described in section (3.2) has been repeating for those new simulations and presented in figure (6 a). Because the  $\Delta\theta = 2^\circ$  simulation is extremely costly, the wave model has been run for 4 months only, from the 1<sup>st</sup> January to the 30<sup>th</sup> April 2015. The altimeters track have been extracted for the same time frame and the model outputs have been interpolated on those track.

Spectral analysis shows that the model set-up with a thinner directional resolution ( $N_\theta = 48$  instead of 24) has a larger variability of  $H_s$  at all scales, with an increase of the PSD by about a factor of 2, similar to what was found for Drake passage by Ardhuin

et al. (2017). Yet, for scales smaller than 100km,  $H_s$  variability is stronger for simulations forced with higher resolution currents, regardless of the directional resolution. Further refining the directional resolution to 180 directions gives a further increase in  $H_s$  variability. When the thin directional discretization is combined with CROCO modeled currents, the modeled  $H_s$  spectrum is within 30% of the satellite measurements for all scales shorter than 100 km.

A typical example of spatial variability along a transect is shown in (Fig. 6.b,c), with a much sharper peak of  $H_s$  in the model runs using 180 or 48 directions.

### 4.3 Influence of incident waves directional spreading ( $\sigma_\theta$ )

We generally expect that a fine directional resolution is most important when the directional wave spectrum is very narrow. In these conditions wave energy can be focused in a small area, as predicted by the analysis of monochromatic waves with rays traced with parallel directions outside of the current region (White & Fornberg, 1998). In contrast, broad wave spectra have focal points in different locations for the different spectral components, which effectively smears the regions of maximum  $H_s$ .

In order to quantify that effect in realistic conditions, we have re-run the model with modified boundary conditions. Instead of taking the directional wave spectra  $E(f, \theta)$  straight from a global hindcast, we now make these spectra broader or narrower in directions, without changing the spreading along the frequency nor the mean direction at each frequency. The details of the method are given in the Appendix. The conservation of the total variance and mean direction between all original spectra and new spectra has been verified. At each frequency, the original directional spreading has been changed by  $\pm 30\%$ . Examples of the resulting  $H_s$  fields are displayed on Figure 7.a-c. Figure 7 illustrates how a decrease  $\sigma_\theta$  induce an increase in the number of small  $H_s$  structures and an amplification of structures already existing, and vice versa. This is better quantified along a track that is close to the upwave (western) boundary. The left peak at  $39.5^\circ$  S in Fig.7.d has a variation of  $H_s$  from 3.45m with a broader spectrum to 3.85 m with a narrower spectrum. This 25% change in wave energy is a typical order of magnitude. Besides the peak, some fluctuations of  $H_s$  between  $37$  and  $39^\circ$  S are much reduced for the broader spectra.

Following the method used previously, we now look at the averaged  $H_s$  spectra for each 1-year long simulation, with different boundary conditions. The result shows higher variability, by about 50%, at all scales for incident waves with lower values of the directional spread  $\sigma_\theta$ . The shape of the  $H_s$  spectra are very similar for all simulations with a steeper slope for wavelengths shorter than 125 km.

Our simulations have confirmed that over a real current system like the Agulhas, the spatial variability is sensitive to the spectral width of the wave field, and to the numerical resolution used in models with narrower spectra and finer resolution producing stronger gradients. Unfortunately the directional spread is one of the worst modeled parameters (Stopa et al., 2016). More directional data, such as provided by the SWIM instrument on the China France Ocean Satellite (Hauser et al., 2017), may help design better model parameterizations and can be used for data assimilation with important impact in strong current regions.

## 5 Conclusion

Surface currents modify the wave field, not just locally (White & Fornberg, 1998; Ardhuin et al., 2017; Kudryavtsev et al., 2017). Large mesoscale systems such as the Agulhas current are places where particularly strong  $H_s$  gradients are found by Quilfen and Chapron (2019). Combining the state of the art of wave modelling and novel filtered al-

timetry data, we have investigated the factors that lead to these large gradients, and under which conditions they can be reproduced by numerical models. The present work shows that model forced with realistic and high resolved surface currents, statistically consistent with the real upper ocean dynamics and sufficiently discretized in direction, is able to capture sharp significant wave height gradient measured by altimeters. Although operational surface currents derived from altimetry-SSH measurement (Globcurrent) describe the overall surface ocean dynamic with a global coverage, the reconstructed global field has a very low spatial resolutions (Ballarotta et al., 2019; Chelton et al., 2019). Indeed, only eddies with diameters of 200 km or more are efficiently resolved because of the space and time sampling of the altimeter tracks and the high along-track noise for scales shorter than 100 km.

Besides the structures of the forcing current, the numerical implementations typically used for wave modelling will typically miss part of the true gradients of the wave field due to numerical diffusion. Here we find that high spectral resolutions, using 48 or more directions systematically produces finer details, in a way that is statistically consistent with altimeter data. This effect is most pronounced when the directional wave spectrum is most narrow. Reproducing realistic wave height gradients is important for marine safety but also for studying upper ocean processes driven by wave breaking. It is also a necessity to capture all sea states bias in surface currents measurement. Finally focus on wave height gradients through model or filtered altimetry data, will be an opportunity to study surface current properties.

More generally, although few observations are available, remote sensing data from SAR or sun glitter imagery or even from the new french chinese satellite CFOSAT should complete this study to draw conclusion on how surface current change the waves height along their tracks. Indeed theories quantify the effect of surface current on the spatial distribution of wave action in random surface currents but there is no clear links between wave height variability and surface currents properties.

## Appendix: Defining new waves spectrum with a modified directional spreading

We force the wave model at its boundaries with bi-dimensional wave spectra from a global hindcast forced without current,  $E(f, \theta)$  with  $f$  the wave intrinsic frequency and  $\theta$  the direction where energy is propagating. Two-dimensional wave spectrum can be divided in an omnidirectional spectrum  $E(f)$  and a directional shape function  $D(f, \theta)$  defined as

$$D(f, \theta) = \frac{E(f, \theta)}{E(f)} \quad (4)$$

such that

$$\int_0^{2\pi} D(f, \theta) d\theta = 1. \quad (5)$$

Our modification of the boundary conditions is done by a modification of  $D(f, \theta)$ , without changing  $E(f)$ .

There can be an infinite number of ways to modify  $D(f, \theta)$ . Here first compute the directional moments  $a_1(f)$ ,  $b_1(f)$ ,  $a_2(f)$ ,  $b_2(f)$  are computed from  $D(f, \theta)$  following O'Reilly et al. (1996). These are the discrete Fourier coefficients of the directional distribution  $D(f, \theta)$ .

From these moments, the following directional parameters have been computed.

$$\left\{ \begin{array}{l} \theta_1 = \arctan(b_1/a_1) \\ \theta_2 = \frac{1}{2} \arctan(b_2/a_2) \\ \sigma_1 = 2 \left( 1 - \sqrt{a_1^2 + b_1^2} \right) \\ \sigma_2 = \frac{1}{2} \left( 1 - \sqrt{a_2^2 + b_2^2} \right) \end{array} \right. \quad \begin{array}{l} (6.a) \\ (6.b) \\ (6.c) \\ (6.d) \end{array}$$

Both directional spreads  $\sigma_1(f)$  and  $\sigma_2(f)$  are multiplied by a parameter  $\alpha$ , giving  $\sigma'_1(f)$  and  $\sigma'_2(f)$ .

From the modified parameters, a new directional distribution  $D'(f, \theta)$  is estimated using the the Maximized Entropy Method (Lygre & Krogstad, 1986).

### Acknowledgments

G.M. is supported by Centre National de l'Etude Spatiale (CNES) and by the Region Bretagne through l'Allocations de recherche doctorale (ARED). Filtered altimeter data are from the European Space Agency Climate Change Initiative Sea State v1 dataset and is freely available on the ESA CCI website (<http://cci.esa.int/data>) at `ftp://anon-ftp.ceda.ac.uk/neodc/esacci/sea_state/data/v1.1_release`. Surface currents derived from altimeters (Globcurrent product) are available in NetCDF format at `ftp://ftp.ifremer.fr/ifremer/ww3/FORCING/GLOBCURGEO/NC4/`. The surface currents simulation from CROCO fully resolved were kindly provided by P. Penven (WOES, Western indian Ocean Energy Sink) and performed as part of the GENCI/IDRIS grant A0040107630. Both fully resolved currents and filtered currents are available at `ftp://ftp.ifremer.fr/ifremer/ww3/FORCING/CROCO/CROCO_AGULHAS/NC4/` in NetCDF format. Authors also thanks M. Accensi for his contribution to the development and maintenance of the WAVEWATCH III model.

### References

- Ardhuin, F., Dumas, F., Bennis, A.-C., Roland, A., Sentchev, A., Forget, P., ... Benoit, M. (2012). Numerical wave modeling in conditions with strong currents: dissipation, refraction and relative wind. *J. Phys. Oceanogr.*, 42, 2101–2120.
- Ardhuin, F., Gille, S. T., Menemenlis, D., Rocha, C. B., Rasche, N., Chapron, B., ... Molemaker, J. (2017). Small scale currents have large effects on wind wave heights. *J. Geophys. Res.*, 122(C6), 4500–4517. doi: 10.1002/2016JC012413
- Ardhuin, F., & Herbers, T. H. C. (2005). Numerical and physical diffusion: Can wave prediction models resolve directional spread? *J. Atmos. Ocean Technol.*, 22(7), 886–895. Retrieved from <http://journals.ametsoc.org/doi/pdf/10.1175/JTECH1723.1>
- Ardhuin, F., Stopa, J. E., Chapron, B., Collard, F., Husson, R., Jensen, R. E., ... Young, I. (2019). Observing sea states. *Frontiers in Marine Sci.*, 6, 124. doi: 10.3389/fmars.2019.00124
- Ballarotta, M., Ubelmann, C., Pujol, M.-I., Taburet, G., Fournier, F., Legeais, J.-F., ... Picot, N. (2019). On the resolutions of ocean altimetry maps. *Ocean Science Discussions*. doi: 10.5194/os-2018-156
- Beal, L. M., Ruijter, W. P. M. D., Biastoch, A., Zahn, R., Cronin, M., Hermes, J., ... Zinke, J. (2011). On the role of the agulhas system in ocean circulation and climate. *Nature*, 472, 429–436. doi: doi:10.1038/nature09983

- Booij, N., Ris, R. C., & Holthuijsen, L. H. (1999, April). A third-generation wave model for coastal regions. 1. model description and validation. *J. Geophys. Res.*, *104*(C4), 7,649–7,666.
- Chelton, D. B., Schlax, M. G., Samelson, R. M., Farrar, J. T., Molemaker, M. J., McWilliams, J. C., & Gula, J. (2019). Prospects for future satellite estimation of small-scale variability of ocean surface velocity and vorticity. *Progress in Oceanography*, *173*, 256–350. doi: 10.1016/j.pocean.2018.10.012
- D’Asaro, E. A. (2014). Turbulence in the upper-ocean mixed layer. *Annu. Rev. Mar. Sci.*, *6*, 101–115. doi: 10.1146/annurev-marine-010213-135138
- Debreu, L., Marchesiello, P., Penven, P., & Cambon, G. (2012). Two-way nesting in split-explicit ocean models: Algorithms, implementation and validation. *Ocean Modelling*, *49*, 1–21. doi: 10.1016/j.ocemod.2012.03.003
- Dibarboure, G., Boy, F., Desjonquieres, J. D., Labroue, S., Lasne, Y., Picot, N., . . . Thibaut, P. (2014). Investigating short-wavelength correlated errors on low-resolution mode altimetry. *J. Atmos. Ocean Technol.*, *31*, 1337–1362. doi: 10.1175/JTECH-D-13-00081.1
- Gula, J., Molemaker, M. J., & McWilliams, J. C. (2015). Gulf stream dynamics along the southeastern u.s. seaboard. *J. Phys. Oceanogr.*, *45*, 690–715.
- Gutshabash, Y. S., & Lavrenov, I. V. (1986). Swell transformation in the cape Agulhas current. *Izv. Atmos. Ocean. Phys.*, *22*(6), 494–497.
- Hauser, D., Tison, C., Amiot, T., Delaye, L., Corcoral, N., & Castellan, P. (2017). SWIM: The first spaceborne wave scatterometer. *IEEE Trans. on Geosci. and Remote Sensing*, *55*(5), 3000–3014.
- Holthuijsen, L. H., & Tolman, H. L. (1991, July). Effects of the Gulf Stream on ocean waves. *J. Geophys. Res.*, *96*(C7), 12755–12771.
- Huang, N. E., Shen, Z., Long, S. R., Wu, M. C., Shih, H. H., Zheng, Q., . . . Liu, H. H. (1998). The empirical mode decomposition and the Hilbert spectrum for nonlinear and non-stationary time series analysis. *Proc. Roy. Soc. Lond. A*, *454*, 903–995.
- Kenyon, K. E. (1971). Wave refraction in ocean current. *Deep Sea Res.*, *18*.
- Komen, G. J., Cavaleri, L., Donelan, M., Hasselmann, K., Hasselmann, S., & Janssen, P. A. E. M. (1994). *Dynamics and modelling of ocean waves*. Cambridge: Cambridge University Press.
- Kudryavtsev, V., Yurovskaya, M., Chapron, B., Collard, F., & Donlon, C. (2017). Sun glitter imagery of surface waves. part 2: Waves transformation on ocean currents. *J. Geophys. Res.*, *122*. doi: 10.1002/2016JC012426
- Landau, L. D., & Lifshitz, E. M. (1960). *Mechanics*. Reading, MA: Pergamon Press Addison-Wesley.
- Longuet-Higgins, M. S. (1957). On the transformation of a continuous spectrum by refraction. *Proceedings of the Cambridge philosophical society*, *53*(1), 226–229.
- Lygre, A., & Krogstad, H. E. (1986). Maximum entropy estimation of the directional distribution in ocean wave spectra. *J. Phys. Oceanogr.*, *16*, 2,052–2,060.
- McWilliams, J. C. (2016). Submesoscale currents in the ocean. *Proc. R. Soc. A*, *427*, 20160117. doi: 10.1098/rspa.2016.0117
- O’Reilly, W. C., & Guza, R. T. (1993). A comparison of two spectral wave models in the Southern California Bight. *Coastal Eng.*, *19*, 263–282.
- O’Reilly, W. C., Herbers, T. H. C., Seymour, R. J., & Guza, R. T. (1996). A comparison of directional buoy and fixed platform measurements of Pacific swell. *J. Atmos. Ocean Technol.*, *13*, 231–238.
- Osborne, A. R., & Burch, T. L. (1980). Coupling between a surface-wave spectrum and an internal wave: modulation interaction. *Science*, *208*(4443), 513–460.
- Phillips, O. M. (1977). *The dynamics of the upper ocean*. London: Cambridge University Press. (336 p.)
- Quilfen, Y., & Chapron, B. (2019). Ocean surface wave-current signatures from satellite altimeter measurements. *Geophys. Res. Lett.*, *216*, 253–261. doi: 10

- .1029/2018GL081029
- Quilfen, Y., Yurovskaya, M., Chapron, B., & Ardhuin, F. (2018). Storm waves sharpening in the Agulhas current: satellite observations and modeling. *Remote sensing of Environment*, 216, 561–571. doi: 10.1016/j.rse.2018.07.020
- Rio, M.-H., Mulet, S., & Picot, N. (2014). Beyond GOCE for the ocean circulation estimate: Synergetic use of altimetry, gravimetry, and in situ data provides new insight into geostrophic and Ekman currents. *Geophys. Res. Lett.*, 41, 8918–8925. doi: 10.1002/2014GL061773
- Sandwell, D. T., Müller, R. D., Smith, W. H. F., Garcia, E., & Francis, R. (2014). New global marine gravity model from cryosat-2 and Jason-1 reveals buried tectonic structure. *Science*, 346, 65–67. doi: 10.1126/science
- Stopa, J. E., Ardhuin, F., Bababin, A., & Zieger, S. (2016). Comparison and validation of physical wave parameterizations in spectral wave models. *Ocean Modelling*, 103, 2–17. doi: 10.1016/j.ocemod.2015.09.003
- Tedesco, P., Gula, J., Ménesguen, C., Penven, P., & Krug, M. (2019). Generation of submesoscale frontal eddies in the agulhas current. *Journal of Geophysical Research*, 124, 7606–7625. doi: 10.1029/2019JC015229
- The WAVEWATCH III<sup>®</sup> Development Group. (2016). *User manual and system documentation of WAVEWATCH III<sup>®</sup> version 5.16* (Tech. Note No. 329). College Park, MD, USA: NOAA/NWS/NCEP/MMAB. (326 pp. + Appendices)
- Tolman, H. L. (1992). Effects of numerics on the physics in a third-generation wind-wave model. *J. Phys. Oceanogr.*, 22, 1095–1111. Retrieved from <http://journals.ametsoc.org/doi/pdf/10.1175/1520-0485%281992%29022%3C1095%3AEONOTP%3E2.0.CO%3B2>
- Tolman, H. L., & Booij, N. (1998). Modeling wind waves using wavenumber-direction spectra and a variable wavenumber grid. *Global Atmos. Ocean Syst.*, 6, 295–309.
- Villas Bôas, A. B., Ardhuin, F., Gommenginger, C., Rodriguez, E., Gille, S. T., Cornuelle, B. D., ... Tsamados, M. (2019). Integrated observations and modeling of winds, currents, and waves: requirements and challenges for the next decade. *Frontiers in Marine Sci.*, submitted.
- Villas Bôas, A. B., & Young, W. R. (2020). Diffusion of surface gravity wave action by mesoscale turbulence at the sea surface. *J. Fluid Mech.*, 890, R3. doi: 10.1017/jfm.2020.116
- Welch, P. D. (1967). The use of fast Fourier transform for the estimation of power spectra: a method based on time averaging over short, modified periodograms. *IEEE Trans. Audio and Electroacoustics*, 15(2), 70–73.
- White, B. S. (1999). Wave action on currents with vorticity. *J. Fluid Mech.*, 386, 329–344.
- White, B. S., & Fornberg, B. (1998). On the chance of freak waves at sea. *J. Fluid Mech.*, 355, 113–138.
- Young, I. R. (1999). *Wind generated ocean waves*. Oxford: Elsevier Science.



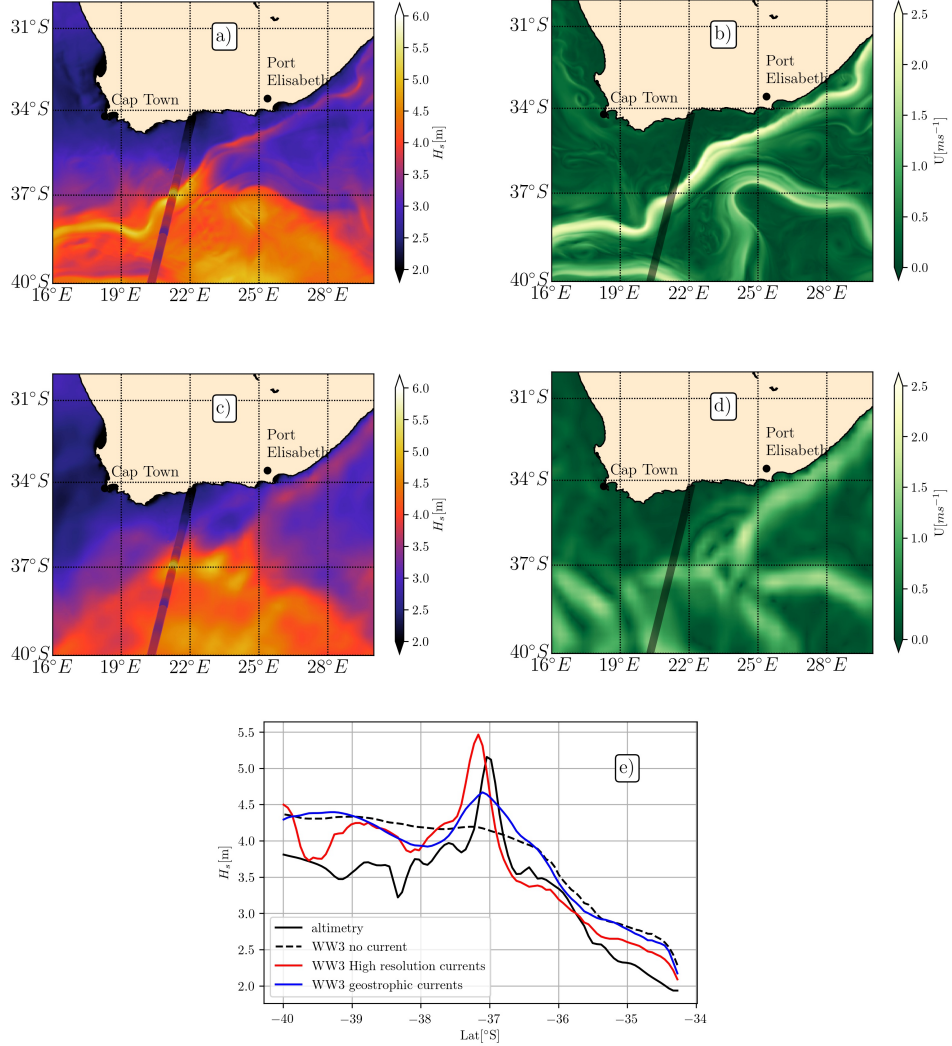


**Figure 1.** Snapshots of modeled  $H_s$  and surface current forcing in the Agulhas system For March 1<sup>st</sup> 2014 at 15:00 UTC. (a) Significant wave height ( $H_s$ ) field computed with the WAVEWATCH III model (WW3) forced with modeled surface current (CROCO 2.5 km resolution shown in (b)), (c)  $H_s$  field computed with WW3 forced with AVISO surface current (derived from satellite altimetry, shown in (c)). (e) along track significant wave height measured by altimeter. The solid black line is the measurement, the red and blue solid lines are  $H_s$  along the altimeter track computed with WW3 using different current forcing, CROCO or AVISO respectively. The dotted black line is the  $H_s$  simulated by the model without surface currents forcing. The altimeter track and the  $H_s$  measurement are also visible on panels a-d.



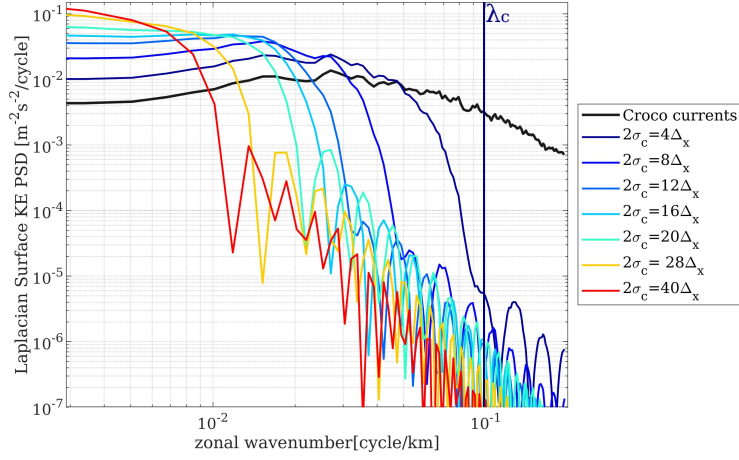


**Figure 2.** Averaged zonal power spectral density (PSD) of the surface Kinetic Energy (KE) laplacian. The widths of the gaussian filters used (two times the gaussian root mean square,  $\sigma_c$ ) are given in the legend in pixel ( $\Delta x$ ). The vertical solid dark blue line is the frequency cut-off for the narrowest gaussian filter.

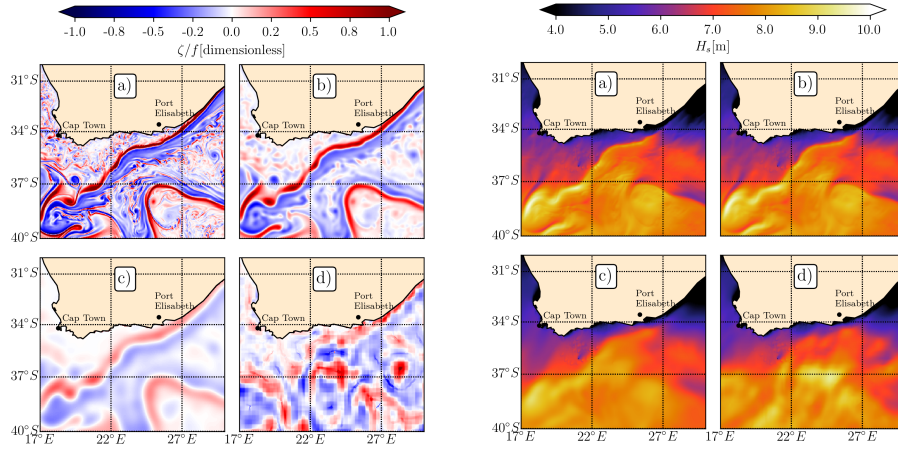


**Figure 3.** (a)-(d) snapshots of normalized vorticity ( $\zeta/f$ ) for currents filtered at  $2.5\text{km}$ ,  $20\text{km}$ ,  $50\text{km}$  and  $150\text{km}$  (Globcurrent surface currents) on August 9<sup>th</sup>, 2015 at 07:00 UTC and (e)-(h) the corresponding  $H_s$  fields.

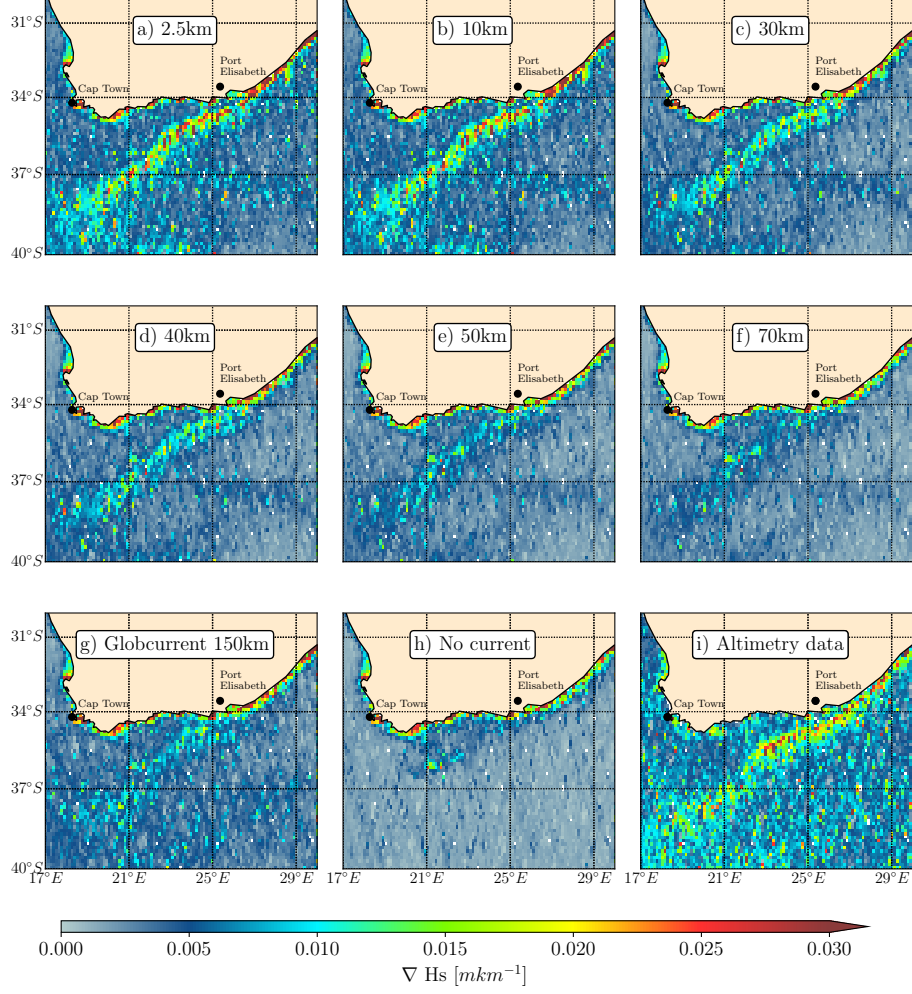


**Figure 4.** Significant wave height gradient from model simulations (a,b,c,d,e,f,g,h) and from altimeters data (i). Simulation with fully resolved CROCO surface currents is represented in a). Simulations forced with filtered surface currents at 10km,30km,40km,50km and 70km effective resolution are displayed in figure b,c,d,e,f respectively. The simulation with geostrophic surface currents from the Globcurrent product is on g) figure and simulation without any surface current forcing is shown in figure h).

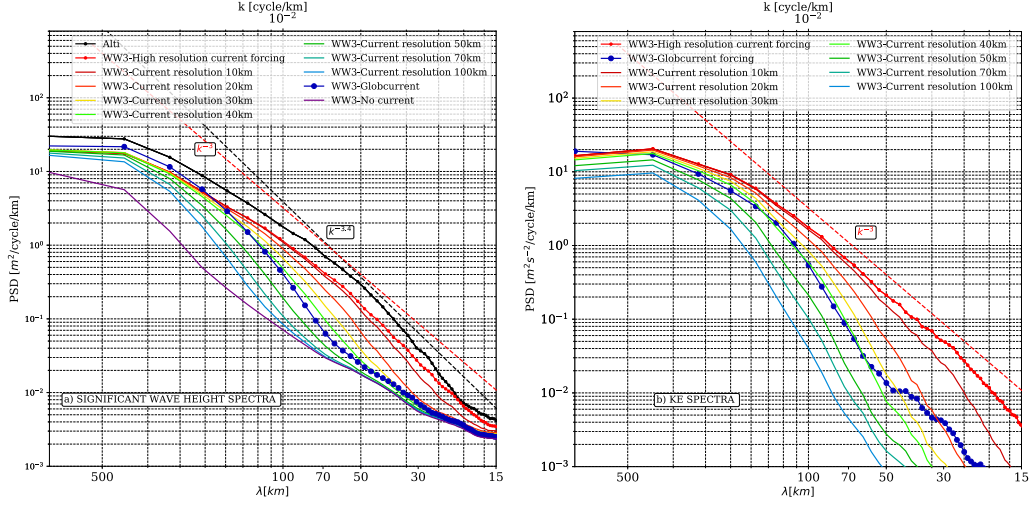


**Figure 5.** Left panel a), averaged Significant Wave Height spectra from model and altimetry data. Right panel b), averaged surface Kinetic Energy spectra. All spectra have been obtained by averaging all along-track spectra (4746 tracks) from altimeters measurements (black solid line) and interpolated simulated data (in colors). The associated surface currents resolution are given in the legend.

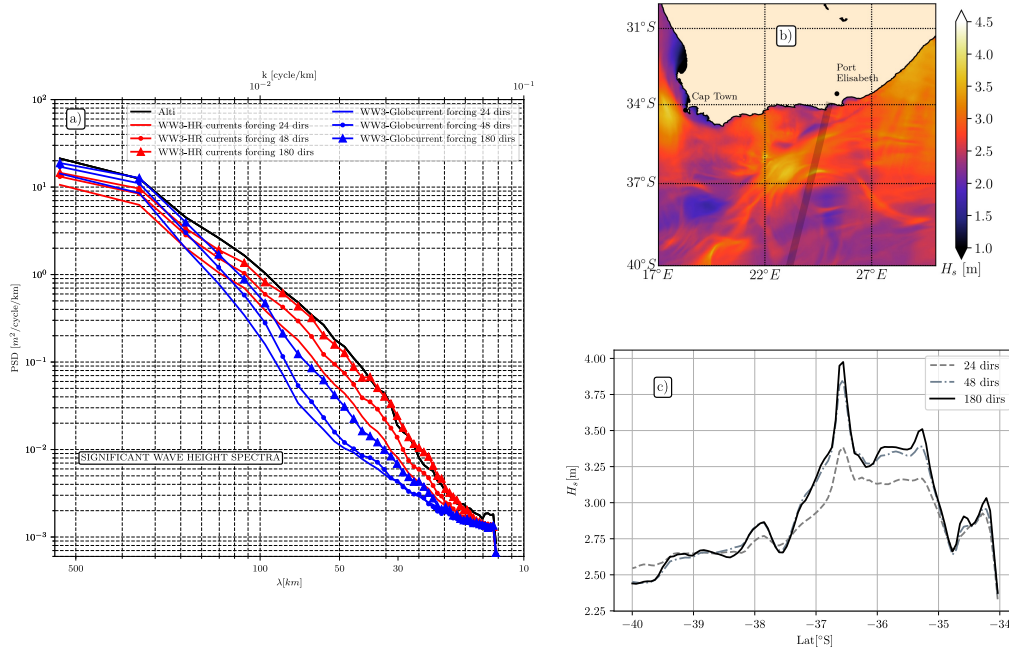


**Figure 6.** a) panel: Averaged Significant Wave Height spectra for altimeters measurements (in black) and for modeled data (colors). Blue spectra are for modeled wave height forced with surface current from Globcurrent and red spectra for CROCO 2.5km forcing. b) instantaneous simulated significant wave height field highly resolved in directions (180 dirs). c) an example of modeled wave heights interpolated along an altimeter track for different directional resolution, the location of the track is in black line on panel b)

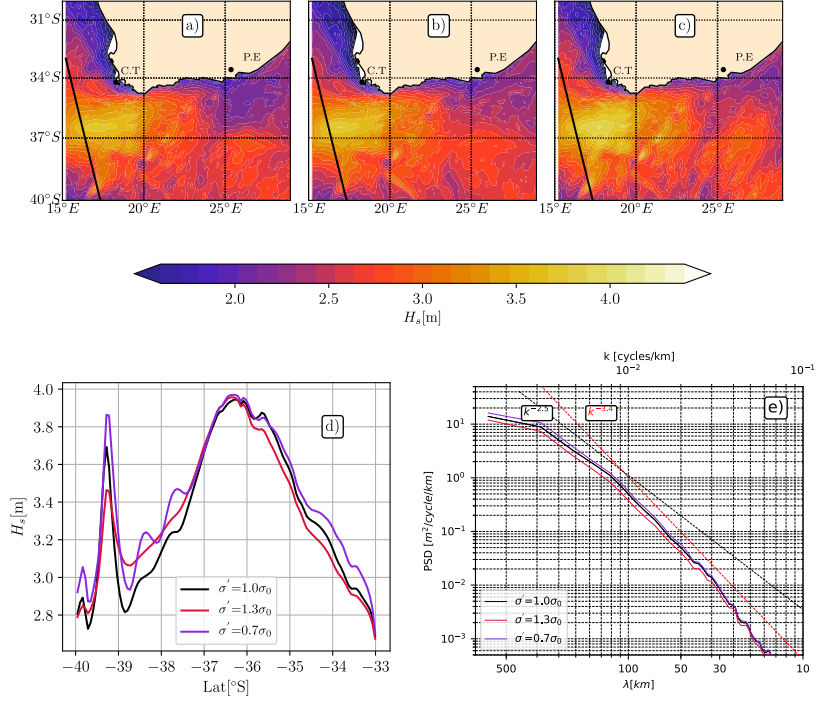


**Figure 7.** Up figures, two dimensional significant wave height field snapshot (November 4<sup>th</sup> 00:00 UTC) for: a) the unchanged directional spreading ( $\sigma_\theta$ ) boundary spectra, b) the extended  $\sigma_\theta$  boundary spectra (+30%), c) the reduced  $\sigma_\theta$  boundary spectra (-30%). The solid line is the footprint of one altimeter track for the same date, the significant waves height simulated are displayed on the d) panel for unmodified (black line), extended (red line) and reduced (purple line)  $\sigma_\theta$ . The e) panel shows the averaged simulated  $H_s$  spectra over one year for the three simulations.